High-resolution Doppler-velocity estimation techniques for processing of coherent heterodyne pulsed lidar data

Ljuan L. Gurdev, Tanja N. Dreischuh, and Dimitar V. Stoyanov

Institute of Electronics, Bulgarian Academy of Sciences, 72 Tzarigradsko Shosse Boulevard, 1784 Sofia, Bulgaria

Received October 22, 1999; revised manuscript received June 9, 2000; accepted July 31, 2000

On the basis of an analysis of the autocovariance of the complex heterodyne signal, some novel algorithms are derived and are investigated for use in determining, with high spatial resolution, Doppler-velocity coherent-lidar profiles in the case of rectangular and rectangularlike sensing laser pulses. These algorithms generalize other known Doppler-velocity estimators for the more complex case of nonuniform scattering and Doppler-velocity distribution within the pulse length. Algorithm performance and efficiency are studied and are illustrated by computer simulations. It is shown that the Doppler-velocity profiles can be determined with essentially better resolution in comparison with the use of other known estimation approaches, but at the expense of some increase in the number of statistical realizations (number of laser shots) required to reduce the speckle-noise effect. The minimum achievable resolution interval is shown to be much shorter than the pulse length.

OCIS codes: 010.0010, 280.3340, 280.3640, 010.3640.

1. INTRODUCTION

The range (spatial) resolution R of pulsed coherent Doppler lidars is usually accepted to be of the order of the pulse length.[1,2] At the same time, the range resolution and the Doppler-velocity resolution (sensitivity) Δv are reciprocally related, and their product is proportional to the wavelength λ of the laser radiation. That is, $R\Delta v = c\lambda/4$, where c is the speed of light. Thus, at a given laser radiation wavelength, the pulse length should exceed some minimum value determined by the minimum Doppler-velocity change to be resolved. So the use of CO_2 laser radiation ($\lambda = 10.6\,\mu$m) has numerous advantages[3,4] and requires a minimum pulse duration of the order of microseconds ($\sim$5.3 μs) for achieving a Doppler-velocity resolution of 1 m/s. Then the corresponding spatial resolution cell along the line of sight is several hundred meters ($\sim$800 m) long. Within such a long-resolution cell, the dispersion of the velocity and concentration of atmospheric particulate matter might be quite large, but the information about it is lost. The use of shorter pulses of shorter-wavelength radiation is a way to improve the range resolution without lowering the velocity resolution, as in the case of employing laser pulses with $\sim$1-μs duration ($\sim$150-m range resolution) and $\lambda \sim 2\,\mu$m.[5–7]

Another approach for improving the range resolution is to develop inverse mathematical techniques for retrieving Doppler-velocity profiles with a considerably shorter resolution cell in comparison with the pulse length. Recently we developed a similar approach concerning the lidar signal power profile.[8,9] It is based on deconvolution techniques for retrieving the so-called short-pulse (δ-pulse) power profile on the basis of the measured power profile and the known pulse shape. In the present study we take a further step: That is, on the basis of an analysis of the autocovariance of the complex heterodyne signal, we develop some novel inverse techniques for improving the coherent-lidar spatial resolution with respect to the Doppler-velocity profile in the case of rectangular and rectangularlike sensing laser pulses. The inverse algorithms obtained generalize other known Doppler-velocity estimators[10,11] for the more complex case of nonuniform scattering and Doppler-velocity distribution within the pulse length. Although the rectangular pulse shape is an idealization, it may be a good approximation of some real laser pulses.[12] Moreover, many features of the techniques developed here, whose feasibility is also tested and illustrated below by computer simulations, should be inherent in similar techniques concerning the cases of more general (or even arbitrary) pulse shapes.

2. COHERENT LIDAR RETURN SIGNAL

The approach considered in this section for the description and modeling of coherent monostatic lidar signals was to our knowledge, first used in Refs. 13 and 14 and was substantiated in Ref. 15. It is described here from a somewhat different point of view in order to make clear the following analysis.

We shall consider the sensing radiation as a sequence of quasi-monochromatic laser pulses with basic (nominal) frequency ω_o, dimensionless temporal amplitude envelope $f_o(\vartheta)$, and some regular frequency deviation (chirp) $\delta\omega_o(\vartheta)$ ($|\delta\omega_o| \ll \omega_o$); ϑ is a time variable, and $f_o(\vartheta) \equiv 0$ for $\vartheta < 0$. Then the expression describing the space–

time amplitude and phase distribution of the sensing laser radiation field $\mathbf{E}_o(\mathbf{r}, t)$ may be written in the form

$$\mathbf{E}_o(\mathbf{r}, t) = \mathcal{P}A(\mathbf{r})f(t - z/c)\exp\left\{j\left[\omega_o(t - z/c) + \int_0^{t-z/c}\delta\omega_o(t'')\mathrm{d}t'' + \phi_o(t - z/c)\right]\right\}, \quad (1)$$

where $\phi_o(\vartheta)$ is a random function describing temporal phase fluctuations, j is imaginary unity, c is the speed of light, t is the time interval after the pulse emission, $\mathcal{P}$ is an in general complex vector characterizing the field polarization state, and $A(\mathbf{r})$ is a space-dependent factor in which, except for the aperture diffraction, the atmospheric influence (extinction, turbulence) along the line of sight is also taken into account (see, e.g., Ref. 16). The line of sight coincides with the axis of the pulsed laser beam. The vector coordinate $\mathbf{r} = \{\boldsymbol{\rho}, z\}$ consists of a transverse vector coordinate $\boldsymbol{\rho}$ and a longitudinal coordinate z with respect to the line of sight, $\boldsymbol{\rho} \equiv 0$ on the beam axis, and $z \equiv 0$ at the transceiver aperture plane.

In the case of linear polarization of the incident laser radiation, $\mathcal{P} \equiv \mathbf{e}$ is a real unit vector. Then the field vector $\mathbf{E}_{bi}[\boldsymbol{\rho}_t, \mathbf{r}_i(t_i'), t]$ of the radiation backscattered by one (say, ith) aerosol particle, at the transceiver aperture plane $\{\boldsymbol{\rho}_t\} \equiv \{\boldsymbol{\rho}_t, 0\}$ and moment t after the pulse emission, is expressible in the form

$$\begin{aligned}\mathbf{E}_{bi}[\boldsymbol{\rho}_t, \mathbf{r}_i(t_i'), t] &= A[\mathbf{r}_i(t_i')]f_o[t - 2z_i(t_i')/c]\exp\left\{j\left[\omega_o[t - 2z_i(t_i')/c] + \int_0^{t-2z_i(t_i')/c}\delta\omega_o(t'')\mathrm{d}t'' + \phi_o[t - 2z_i(t_i')/c]\right]\right\} \\ &\times \mathbf{a}_i[\mathbf{r}_i(t_i')]G_\perp[\boldsymbol{\rho}_t; \mathbf{r}_i(t_i')], \end{aligned} \quad (2)$$

where $\mathbf{r}_i(t') \equiv \{\boldsymbol{\rho}_i(t'), z_i(t')\}$ is the vector coordinate of the scattering particle at the corresponding earlier moment of interaction t_i', $\mathbf{a}_i$ is the scattering amplitude of the particle,[17] and $G[\boldsymbol{\rho}_t; \mathbf{r}_i] = G_\perp[\boldsymbol{\rho}_t; \mathbf{r}_i]\exp(-j\omega_o z_i/c)$ is the paraxially approximated Green function used for description of the backscattered-wave propagation in the atmosphere, taking into account in general the extinction and turbulence effects.[16] Under single-scattering conditions, the total backscattering field $\mathbf{E}_b(\boldsymbol{\rho}_t, t)$ is a superposition of the elementary wave fields backscattered by the scatterers that contribute to the signal. That is,

$$\mathbf{E}_b(\boldsymbol{\rho}_t, t) = \sum_i \mathbf{E}_{bi}[\boldsymbol{\rho}_i, \mathbf{r}_i(t_i'), t]. \quad (3)$$

The equivalent local-oscillator field vector $\mathbf{E}_h(\boldsymbol{\rho}_t, t)$ at the transceiver aperture plane can be given in the form

$$\mathbf{E}_h(\boldsymbol{\rho}_t, t) = \mathbf{A}_h(\boldsymbol{\rho}_t)\exp\{j[\omega_h t + \phi_h(t)]\}, \quad (4)$$

where $\mathbf{A}_h(\boldsymbol{\rho}_t)$ is the spatially dependent (complex amplitude) factor, ω_h is the optical heterodyne frequency, and $\phi_h(t)$ is a function describing phase fluctuations.

When the photodetector collects all the local-oscillator beam energy and all the backscattered radiation that is covered by the receiving optical system, the complex photocurrent $I(t)$ resulting from coherent heterodyne detection may be represented as[18]

$$I(t) = J(t) + jQ(t) = K\int \mathbf{E}_b(\boldsymbol{\rho}_t, t) \cdot \mathbf{E}_h^*(\boldsymbol{\rho}_t, t)\mathrm{d}\boldsymbol{\rho}_t, \quad (5)$$

where $K = 2qe/\hbar\omega$, q is the photodetector (uniform) quantum efficiently, e is the electron charge, $\hbar = h/2\pi$, h is the Planck constant, $\omega = (\omega_o + \omega_h)/2$, and superscript $*$ denotes complex conjugation. Functions $J(t)$ and $Q(t)$ are, respectively, in-phase and quadrature components of $I(t)$. On the basis of Eqs. (2)–(5) we obtain the following explicit expression of $I(t)$:

$$\begin{aligned} I(t) &= K\exp[j(\omega_o - \omega_h)t - \phi_h(t)]\sum_i \mathbf{a}_i A[\mathbf{r}_i(t_i')] \\ &\times f_o[t - 2z_i(t_i')/c]\exp\left\{j\left[-2\omega_o z_i(t_i')/c + \int_0^{t-2z_i(t_i')/c}\delta\omega_o(t'')\mathrm{d}t'' + \phi_o[t - 2z_i(t_i')/c]\right]\right\} \\ &\cdot \int \mathbf{A}_h^*(\boldsymbol{\rho}_t)G_\perp[\boldsymbol{\rho}_t; \mathbf{r}_i(t_i')]\mathrm{d}\boldsymbol{\rho}_t. \end{aligned} \quad (6)$$

One can assume that when interacting with a propagating (sensing) laser pulse, each (ith) scatterer moves with a constant radial velocity $v_i \ll c$. Then one can derive the Doppler frequency shift on the basis of classical considerations by representing $z_i(t_i')$ in the exponent in Eq. (6) as $z_i(t_i') = z_{io} + v_i(t - 2z_{io}/c)$, where z_{io} is the longitudinal position of the particle when it is met by the pulse front. The corresponding total vector coordinate is $\mathbf{r}_{io} \equiv \{\boldsymbol{\rho}_{io}, z_{io}\}$. Factors A and $G_\perp$ in Eq. (6) also depend, in general, on the particle motion as $\mathbf{r}_i(t_i') = \mathbf{r}_{io} + \mathbf{v}_i(t - 2z_{io}/c)$. Here $\mathbf{v}_i = \{\mathbf{v}_{Ti}, v_i\}$ is the total vector of the scatterer velocity with transverse component $\mathbf{v}_{Ti}$. According to the results of Ref. 19 (see also Ref. 20), the indicated dependence does not influence the temporal autocovariance of $I(t)$ (which is of interest in what follows) when the inequalities $v_T\tau/a \ll 1$ and $\pi a v_T\tau/(\lambda z) \ll 1$ are satisfied; $v_T = |\mathbf{v}_T|$, τ is the pulse duration, and a is the laser beam radius. Since these inequalities are usually satisfied for coherent lidars, we shall neglect the effect of the scatterer motion on A and $G_\perp$. Thus Eq. (6) may be rewritten in the form

$$\begin{aligned} I(t) &= K\exp[-j\phi_h(t)]\sum_i \mathbf{a}_i A(\mathbf{r}_i)f_o(t - 2z_i/c) \\ &\times \exp(-2jk_{Di}z_{io}) \\ &\times \exp(j\{\omega_{mi}t + \phi_{\mathrm{ch}}[(t - 2z_{io}/c)\chi_i] + \phi_o[(t - 2z_{io}/c)\chi_i]\}) \\ &\cdot \int \mathbf{A}_h^*(\boldsymbol{\rho}_t)G_\perp[\boldsymbol{\rho}_t; \mathbf{r}_i(t_i')]\mathrm{d}\boldsymbol{\rho}_t, \end{aligned} \quad (7)$$

where $\omega_{mi} = \omega_{Di} - \omega_h$ is the intermediate frequency, $\omega_{Di} = \omega_o\chi_i$ is the Doppler-shifted frequency and $k_{Di} = \omega_{Di}/c$ is the corresponding wave number, $\chi_i = 1 - 2v_i/c$, and

$$\phi_{\mathrm{ch}}[(t - 2z_{io}/c)\chi_i] = \int_0^{(t-2z_{io}/c)\chi_i} \delta\omega_o(t'')\mathrm{d}t''$$

is the phase increment due to the chirp. Consider the semispace $\{z \geqslant 0\}$ as consisting of plane slices with thickness $\Delta z_o = c\Delta t_o/2$ that are perpendicular to the line of sight. The slice thickness Δz_o may in practice be equal to the spatial sampling interval along the line of sight that corresponds to a temporal sampling interval Δt_o. We shall assume that Δz_o is large compared with the wavelength $\lambda = 2\pi c/\omega_o$ but that it is sufficiently small that within each (lth) slice $[(l-1)\Delta z_o \leqslant z \leqslant l\Delta z_o]$ functions ϕ_{ch}, ϕ_o, A, $G_\perp$, and certainly f do not change with z, and the scattering particles have uniform radial velocity $v(z_l)$. The scatterers contributing to the signal may be numbered within every lth slice by an additional (except l) index n (l, $n = 1, 2, \ldots$). So instead of Eq. (7) we can write

$$I(t) = K\exp[-j\phi_h(t)]\sum_l f_o(t - 2z_l/c) \times \exp(j\{\omega_{ml}t + \phi_{\mathrm{ch}}[(t - 2z_l/c)\chi_l] + \phi_o[(t - 2z_l/c)\chi_l]\})\mathrm{d}\mathcal{A}(z_l), \quad (8)$$

where $z_l = l\Delta z_o$, $\omega_{ml} = \omega_o\chi_l - \omega_h$, $\chi_l = 1 - 2v(z_l)/c$,

$$\mathrm{d}\mathcal{A}(z_l) = \sum_n \exp(-2jk_{Dl}z_{oln})A(\boldsymbol{\rho}_{ln}, z_l)\mathbf{a}_{nl} \cdot \int \mathbf{A}_h^*(\boldsymbol{\rho}_t)G_\perp(\boldsymbol{\rho}_t; \boldsymbol{\rho}_{ln}, z_l)\mathrm{d}\boldsymbol{\rho}_t, \quad (9)$$

$\boldsymbol{\rho}_{ln}$ and z_{oln} are coordinates concerning the nth particle inside the lth slice, $\mathbf{a}_{nl}$ is the corresponding scattering amplitude, and $k_{Dl} = \omega_o\chi_l/c$.

The aerosol scatterers have a quite random mutual disposition that conditions the incoherent character of the scattering process. In this case, when the single backscattering prevails $\mathrm{d}\mathcal{A}(z_l) = \mathrm{d}\mathcal{A}_r(z_l) + j\mathrm{d}\mathcal{A}_j(z_l)$ is a circular complex Gaussian random quantity.[21] The distributions of $\mathrm{d}\mathcal{A}_r(z_l)$ and $\mathrm{d}\mathcal{A}_j(z_l)$ are identical Gaussian ones with zero mean value and variance $D[\mathrm{d}\mathcal{A}_{r,j}(z_l)] = \langle[\mathrm{d}\mathcal{A}_r(z_l)]^2\rangle = \langle[\mathrm{d}\mathcal{A}_j(z_l)]^2\rangle$, where $\langle\cdot\rangle$ denotes ensemble average. Also, $\mathrm{d}\mathcal{A}_r(z_l)$ and $\mathrm{d}\mathcal{A}_j(z_l)$ are statistically uncorrelated; i.e., $\langle\mathrm{d}\mathcal{A}_r(z_l)\mathrm{d}\mathcal{A}_j(z_l)\rangle = 0$. Because of the incoherent scattering, the contributions of different slices to the heterodyne signal are also uncorrelated, and correspondingly $\langle\mathrm{d}\mathcal{A}(z_l)\mathrm{d}\mathcal{A}(z_{l+s})\rangle = 0$ when $s \neq 0$ ($s = \pm1, \pm2, \ldots$). The value of $\mathrm{d}\mathcal{A}(z_l)$ can be represented in the form

$$\mathrm{d}\mathcal{A}(z_l) = \Phi_o^{1/2}(z_l)(\Delta z_o)^{1/2}w_l, \quad (10)$$

where

$$\Phi_o(z_l)(\Delta z_o) = \langle|\mathrm{d}\mathcal{A}(z_l)|^2\rangle = D[\mathrm{d}\mathcal{A}_r(z_l)] + D[\mathrm{d}\mathcal{A}_j(z_l)]$$

is the variance of $\mathrm{d}\mathcal{A}(z_l)$, and $w_l = w = w_r + jw_j$ is a complex Gaussian random quantity with zero mean value $\langle w\rangle = \langle w_r\rangle = \langle w_j\rangle = 0$ and unitary variance $Dw = \langle|w|^2\rangle = \langle w_r^2\rangle + \langle w_j^2\rangle = 1$. $Dw_r = \langle w_r^2\rangle = Dw_j = \langle w_j^2\rangle$, $\langle w_r w_j\rangle = 0$, and $\langle w_l w_{l+s}\rangle = 0$ for $s \neq 0$. Taking into account the properties of $\mathrm{d}\mathcal{A}(z_l)$, the mean heterodyne signal power $P(t) = \langle|I(t)|^2\rangle$ is obtainable from Eq. (8) in the form of the following sum,

$$P(t) = \sum_{l=l_1+1}^{l_2} f(t - 2z_l/c)\Phi(z_l)\Delta z_o \quad (11a)$$

or integral

$$P(t) = \int_{\phi(t)}^{ct/2} f(t - 2z/c)\Phi(z)\mathrm{d}z, \quad (11b)$$

where $f = f_o^2$ and $\Phi(z) = K^2\Phi_o(z)$. Thus the quantity $\Phi(z)$ characterizes the contribution to the heterodyne signal power of unitary length along the line of sight at unit f. The function $f(\vartheta) = P_{\mathrm{imp}}(\vartheta)/P_p$ describes the pulse power shape $P_{\mathrm{imp}}(\vartheta) = \int\mathbf{E}_o(\boldsymbol{\rho}_t, \vartheta)\cdot\mathbf{E}_o^*(\boldsymbol{\rho}_t, \vartheta)\mathrm{d}\boldsymbol{\rho}_t$ normalized to its peak value $P_p = \int\mathcal{A}(\boldsymbol{\rho}_t)A^*(\boldsymbol{\rho}_t)\mathrm{d}\boldsymbol{\rho}_t$ [see Eq. (1) with $\mathbf{r} \equiv \boldsymbol{\rho}_t$, $t \equiv \vartheta$, and $\boldsymbol{\mathcal{P}} = \mathbf{e}$]. Correspondingly, the pulse energy $E_{\mathrm{imp}} = \int_0^\infty P_{\mathrm{imp}}(\vartheta)\mathrm{d}\vartheta = P_p\tau$, where $\tau = \int_0^\infty f(\vartheta)\mathrm{d}\vartheta$ is the effective pulse duration ($l_p = c\tau$ is then the effective pulse length). According to Eqs. (11a) and (11b), the value of $\Phi(z)$ [or $\Phi(z_l)$] is proportional to the maximum-resolved (short-pulse) signal power profile $P_m(t = 2z/c) = (c\tau/2)\Phi(z)$ that is obtainable by sufficiently short sensing pulses (physical δ pulses). In the case of a restricted pulse shape with actual duration τ_a [when $f(\vartheta \notin [0, \tau_a]) \equiv 0$], in Eqs. (11a) and (11b) we have $l_1 = c(t - \tau_a)/(2\Delta z_o)$, $l_2 = ct/(2\Delta z_o)$, and $\phi(t) = c(t - \tau_a)/2$. In the case of pulse shape with asymptotically falling tail, $l_1 = z_o/\Delta z_o$, $l_2 = ct/(2\Delta z_o)$, and $\phi(t) = z_o$. The range from $z = 0$ to $z = z_o$ is the lidar dead zone. The backscattered radiation from this zone is not detectable because, for example, there is no overlapping between the sensing laser beam and the field of view of the receiving optical system.[22]

Taking into account Eq. (10), we can rewrite Eq. (8) in the following forms:

$$I(t) = \exp[-j\phi_h(t)]\sum_{l=l_1+1}^{l_2}[f(t - 2z_l/c)\Phi(z_l)\Delta z_o]^{1/2} \times w(z_l)\exp\{j\omega_{ml}t + j\phi_{\mathrm{ch}}[(t - 2z_l/c)\chi_l] + j\phi_o[(t - 2z_l/c)\chi_l]\}, \quad (12a)$$

or

$$I(t) = \exp[-j\phi_h(t)]\int_{\phi(t)}^{ct/2}[f(t - 2z/c)]^{1/2} \times \exp\{j\omega_m(z)t + j\phi_{\mathrm{ch}}[(t - 2z/c)\chi(z)] + j\phi_o[(t - 2z/c)\chi(z)]\}\mathrm{d}\mathcal{A}(z), \quad (12b)$$

where

$$\langle\mathrm{d}\mathcal{A}(z)\mathrm{d}\mathcal{A}(z')\rangle = \Phi(z)\delta(z - z')\mathrm{d}z\,\mathrm{d}z',$$

$$\omega_m(z) = \omega_o\chi(z) - \omega_h, \ \chi(z) = 1 - 2v(z)/c,$$

and ϕ_o is assumed to be stable within a slice.

3. AUTOCOVARIANCE OF THE COHERENT LIDAR RETURN SIGNAL

On the basis of Eq. (12a) or Eq. (12b), assuming that the value of ϕ_h is stable within a pulse duration, we obtain the following expression of the autocovariance function of the coherent lidar signal:

$$\begin{aligned}\mathrm{Cov}(t,\theta) &= \langle I^*(t)I(t+\theta)\rangle \\ &= \int_{\phi(t+\theta)}^{ct/2} \mathrm{d}z f_o(t-2z/c) f_o(t+\theta-2z/c)\Phi(z) \\ &\quad \times \exp\{j[\omega_m(z)\theta + \Delta\phi_{\mathrm{ch}}(t,\theta,z)]\} \\ &\quad \times \xi(t,\theta,z)\gamma_z(2\omega_o\theta/c), \end{aligned} \tag{13a}$$

where $\theta \geqslant 0$ is a time shift,

$$\Delta\phi_{\mathrm{ch}}(t,\theta,z) = \phi_{\mathrm{ch}}[(t-2z/c)\chi(z)] - \phi_{\mathrm{ch}}[(t+\theta-2z/c)\chi(z)],$$

$$\xi(t,\theta,z) = \langle \exp\{j\phi_o[(t-2z/c)\chi(z)] - j\phi_o[(t+\theta-2z/c)\chi(z)]\}\rangle,$$

and

$$\gamma_z(y) = \int \exp[-jy\tilde{v}(z)]p[\tilde{v}(z)]\mathrm{d}\tilde{v}$$

is the characteristic function corresponding to the probability density distribution $p[\tilde{v}(z)]$ of the radial velocity fluctuations $\tilde{v}(z)$. Here we consider $v(z)$ as ensemble-mean value of the radial velocity and $v_r(z) = v(z) + \tilde{v}(z)$ as a random realization of it. The influence of the Brownian velocity dispersion is neglected, and all the scattering particles in a slice are assumed to have uniform velocity fluctuations. If the regular chirp effect and the phase fluctuations are negligible, at a τ-long rectangular pulse $\{f(t) = 1$ for $t \in [0,\tau]$ and $f(t) = 0$ elsewhere$\}$ Eq. (13a) acquires the form

$$\mathrm{Cov}(t,\theta) = \int_{c(t+\theta-\tau)/2}^{ct/2} \mathrm{d}z\Phi(z)\exp[j\omega_m(z)\theta]\gamma_z(2\omega_o\theta/c). \tag{13b}$$

$\mathrm{Cov}(t,\theta)$ is a complex function with a real part

$$\mathrm{Re\ Cov}(t,\theta) = \langle J(t)J(t+\theta)\rangle + \langle Q(t)Q(t+\theta)\rangle$$

and an imaginary part

$$\mathrm{Im\ Cov}(t,\theta) = \langle J(t)Q(t+\theta)\rangle - \langle J(t+\theta)Q(t)\rangle.$$

At $\theta = 0$, from Eq. (13b) we obtain

$$\mathrm{Cov}(t,\theta) = P(t) = \int_{c(t-\tau)/2}^{ct/2} \Phi(z)\mathrm{d}z. \tag{13c}$$

4. RETRIEVING $v(z)$ WITH HIGH RESOLUTION

On the basis of Eq. (13b) we first determine the expressions of the covariance derivatives $\mathrm{Cov}'_t(t,\theta)$ (first derivative with respect to t) and $\mathrm{Cov}''_{t\theta}(t,\theta=0)$ (second mixed derivative with respect to t and θ at $\theta = 0$). Then we derive from the expressions obtained [of $\mathrm{Cov}'_t(t,\theta)$ and $\mathrm{Cov}''_{t\theta}(t,\theta=0)$] the following two relations for determination of $\omega_m(z)$ [respectively, $v(z)$] that are certainly valid only for (informative) line-of-sight regions containing scatterers [where $\Phi(z = ct/2) \neq 0$]:

$$\begin{aligned}\omega_m(z=ct/2) = \{&\Phi[c(t-\tau)/2]\omega_m[c(t-\tau)/2] \\ &+ \mathrm{Im}[(2/c)\mathrm{Cov}''_{t\theta}(t,\theta=0)]\} \\ &\times [\Phi(ct/2)]^{-1}, \end{aligned} \tag{14a}$$

$$\omega_m(z=ct/2) = \theta^{-1} \times \arctan\left(\frac{(2/c)\mathrm{Im\ Cov}'_t(t,\theta) + \Phi[c(t+\theta-\tau)/2]\gamma\sin\{\omega_m[c(t+\theta-\tau)/2]\theta\}}{(2/c)\mathrm{Re\ Cov}'_t(t,\theta) + \Phi[c(t+\theta-\tau)/2]\gamma\cos\{\omega_m[c(t+\theta-\tau)/2]\theta\}}\right), \tag{14b}$$

where $\gamma = \gamma[z = c(t+\theta-\tau)/2;\ 2\omega_o\theta/c]$ and the quantities $ct/2$, $[c(t-\tau)/2]$, and $[c(t+\theta-\tau)/2]$ are arguments of the functions Φ and ω_m. It can be seen that the second relation obtained [formula (14b)] depends explicitly on the velocity-fluctuation characteristic function $\gamma_z(2\omega_o\theta/c) \equiv \gamma(z;\ 2\omega_o\theta/c)$, which is in addition assumed here [only when deriving Eq. (14b)] to be a real function corresponding to some symmetric probability density distribution $p(\tilde{v}) = p(-\tilde{v})$. The last assumption is in accordance, for example, with the conception of locally homogeneous and isotropic (statistically) turbulent velocity fluctuations (see, e.g., Ref. 23). Thus it turns out that formula (14b) is effective only when $\omega_o\theta\sigma/c \ll 1$ or $z - z_o < c(\tau-\theta)/2$, where $\sigma = \langle\tilde{v}^2\rangle^{1/2}$ is the root-mean-square value of the velocity fluctuations. In the latter case

$$\omega_m(z=ct/2) = \theta^{-1}\arctan[\mathrm{Im\ Cov}'_t(t,\theta)/\mathrm{Re\ Cov}'_t(t,\theta)], \tag{14c}$$

which means that at sufficiently long sensing pulses or lidar dead zone $[0, z_o]$, one could determine ω_m at long distances z without any prior (*a priori*) information about $\gamma_z(2\omega_o\theta/c)$.

In the cases when $\Phi(z)$ and $\omega_m(z)$ are practically constant within every $c\tau/2$-long spatial interval, Eq. (13b) leads to the algorithms

$$\omega_m(z=ct/2) = [\mathrm{Im\ Cov}'_\theta(t,\theta=0)]/\mathrm{Cov}(t,\theta=0), \tag{15a}$$

$$\omega_m(z=ct/2) = \theta^{-1}\arctan[\mathrm{Im\ Cov}(t,\theta)/\mathrm{Re\ Cov}(t,\theta)], \tag{15b}$$

where the first one has been investigated by us formerly[10] and the second one is the well-known pulse-pair (PP) algorithm.[11] Thus, formulas (14a)–(14c) generalize the known algorithms (15a) and (15b) for the more complex case of nonuniform distributions of $\Phi(z)$ and $\omega_m(z)$ within the pulse length.

The resolution step achievable by algorithms (14a)–(14c) may be considerably shorter than $c\tau/2$ and even of

the order of the sampling interval. In this case $\mathrm{Cov}(t, \theta)$ is determined by a "true" ensemble averaging over a sufficiently large number of laser shots to suppress the noise effects (see below in Section 5). In this way the signal power profile $P(t)$ is also determined because $P(t) = \mathrm{Cov}(t, \theta = 0)$. The short-pulse signal power profile $\Phi(z = ct/2)$ is then obtained (by the deconvolution technique[8]) as a solution of Eq. (13c). The PP algorithm makes use in practice of a temporal averaging (along the line of sight) on the basis of one realization (or some relatively small number of realizations) of the random process $I(t)$ assumed to be the locally stationary and ergodic one. This allows one to achieve a fast result but lowers the spatial resolution because the resolution cell becomes longer than $c\tau/2$.

5. SIMULATIONS

The algorithm performance has been simulated by use of various distributions of the radial velocity $v(z)$ and the mean signal power $\propto \Phi(z)$. Below we present results for two models of $v(z)$. The first model is (see also Fig. 1)

$$v(z) = v(z - z_o) = v_1(z)\sin\{4\pi(z - z_o)/[q_1\lambda + q_2(z - z_o)]\} + v_o, \tag{16}$$

where

$$v_1(z) = q_3(z - z_o)/(z_s - z_o) + q_4,$$
$$q_1 = 1.5 \times 10^8, \quad q_2 = 0.3, \quad q_3 = 10\ \mathrm{m/s},$$
$$q_4 = 3\ \mathrm{m/s}, \quad v_o = 3\ \mathrm{m/s}, \quad z_s = 8700\ \mathrm{m}.$$

This model is like an alternating wind velocity profile and is intended for investigating the algorithm performance over relatively large ranges along the line of sight. The corresponding model used of $\Phi(z)$ is (see Fig. 2)

$$\Phi(z = ct/2) = W\begin{cases} 0 & \text{for } t \le t_o \\ B_1(t - t_o)^{-3}\exp[-B_2/(t - t_o)] + B_3\sin^2[2\pi(t - t_o)/T] & \text{for } t_o < t \le B_2 + t_o \\ B_1(t - t_o)^{-3}\exp[-B_2/(t - t_o)] & \text{for } t > B_2 + t_o \end{cases} \tag{17}$$

where W is a system constant, $B_1 = 3000\,\mu\mathrm{s}^3$, $B_2 = 20\,\mu\mathrm{s}$, $B_3 = 0.1$, and $T = 10\,\mu\mathrm{s}$. At a laser radiation wavelength assumed as $\lambda = 10.6\,\mu\mathrm{m}$, the temporal sampling interval $\Delta t_o = 2\Delta z_o/c$, the pulse duration $\tau = l_p/c$, and the initial moment of signal registration $t_o = 2z_o/c$ may have various values; Δz_o and l_p are the spatial sampling interval and the pulse length, respectively. The concrete values concerning the models shown in Figs. 1 and 2 are $\Delta t_o = 0.1\,\mu\mathrm{s}$ ($\Delta z_o = 15\,\mathrm{m}$), $\tau = 4\,\mu\mathrm{s}$ ($l_p = 1200\,\mathrm{m}$), and $t_o = 2\,\mu\mathrm{s}$ ($z_o = 300\,\mathrm{m}$).

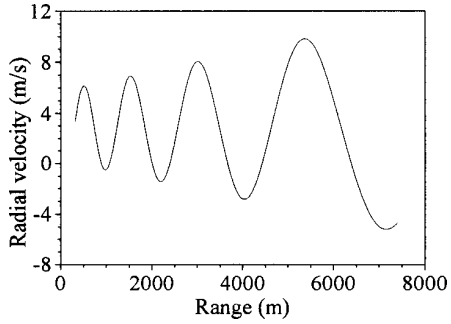

Fig. 1. Model of the alternating radial wind-velocity profile [Eq. (16)] as a function of range.

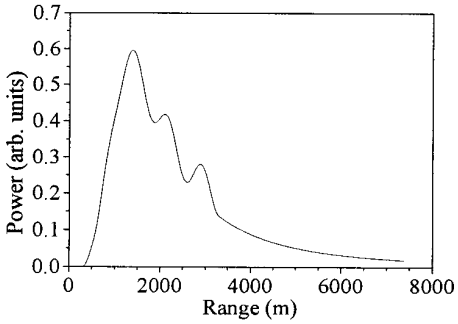

Fig. 2. Model of the maximum-resolved signal power profile $\Phi(z)$ used in the simulations of the case of alternating wind velocity profile.

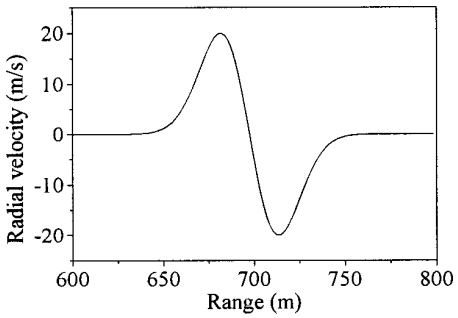

Fig. 3. Model of the wind-vortex-like distribution [Eq. (18)] of the radial (Doppler) velocity along the line of sight.

The second model of $v(z)$ is (see Fig. 3)

$$v(z) = C[(z - z_o) - a]\exp\{-[(z - z_o) - a]^2/b^2\}/b^2, \tag{18}$$

where $a = 97.5\,\mathrm{m}$, $b = 22.5\,\mathrm{m}$, and $C = -1050\,\mathrm{m}^2/\mathrm{s}$. It describes a wind-vortex-like distribution of the radial velocity $v(z)$. Such a distribution is characterized by small spatial size and sharp velocity variations.[5,15] Therefore it is convenient for investigating (by simulations) the high-resolution performance potential of algorithms (14a) and (14b). The temporal sampling interval here is chosen to be $\Delta t_o = 0.01\,\mu\mathrm{s}$ ($\Delta z_o = 1, 5\,\mathrm{m}$). The pulse durations used in the simulations are $\tau = 200\,\mathrm{ns}$ ($l_p = 60\,\mathrm{m}$) at $\lambda = 2\,\mu\mathrm{m}$ and $\tau = 4\,\mu\mathrm{s}$ ($l_p = 1200\,\mathrm{m}$) at $\lambda = 10.6\,\mu\mathrm{m}$. As above, the initial moment t_o of signal

registration may have various values. The model used here of $\Phi(z)$ is given again by Eq. (17) but with a new set of constants ($B_1 = 20\,\mu s^3$, $B_2 = 3.5\,\mu s$, $B_3 = 0.05$, and $T = 1\,\mu s$).

The coherent-lidar return signal $I(t) = J(t) + jQ(t)$ is simulated according to Eqs. (12a) and (12b) (with $\phi_h = \phi_{ch} = \phi_o = 0$, $\bar{v} = 0$, and $\omega_o = \omega_h$), where the complex random variable $w = w_r + jw_j$ (i.e., w_r and w_j) should be generated in an appropriate way. We have solved this task by using the method described in Ref. 24. As a test, we have compared the probability density distribution of the random quantity $|I(t)|^2/P(t)$ (the signal power normalized to its mean value) with the corresponding expected negative exponential distribution.[21] As is seen in Fig. 4, the coincidence is satisfactory. A pair of realizations of the in-phase $J(t)$ and the quadrature $Q(t)$ components of the signal are given, for example, in Fig. 5, for the case of the first Doppler-velocity model described above [Eq. (16)]. The covariance estimates $\widehat{\mathrm{Cov}}(t, \theta)$ are obtained on the basis of the relation

$$\widehat{\mathrm{Cov}}(t = t_{l_2} = 2z_{l_2}/c, \theta = m\Delta t_o) = N^{-1}\sum_{k=1}^{N} I_k^*(t_{l_2}) I_k(t_{l_2} + m\Delta t_o), \quad (19)$$

where N is the number of realizations employed, $I_k(t)$. The same relation, at $m = 0$, provides the signal power profile estimates $\hat{P}(t) = \widehat{\mathrm{Cov}}(t, \theta = 0)$. Then the estimates $\hat{\Phi}(z = ct/2)$ of the short-pulse signal power profile $\Phi(z = ct/2)$ are obtained (by deconvolution[8]) as the solution of Eq. (13c) with $P(t) = \hat{P}(t)$. This solution has the form $\hat{\Phi}(z = ct/2) = \hat{\Phi}[z = c(t - \tau)/2] + (2/c)\hat{P}_t'(t)$, $\hat{\Phi}(z \leqslant z_o) = 0$. The simulations performed show that, for instance, an additive noise at signal-to-noise ratio S/N (defined as, e.g., in Ref. 25) of the order of 100, at maximum signal power, does not have a noticeable effect on the final results when $N = 500$. Therefore, we have investigated mainly the influence of speckle noise on algorithm performance. A reduction of the influence of noise is achieved by using sufficiently large statistical ensembles of realizations $I_k(t)$ and smoothing the covariance estimates and the recovered Doppler-velocity profiles $v_r(z)$. We do not consider the influence of the frequency chirp on the final results; that is, we assume that the chirp effect is negligible.

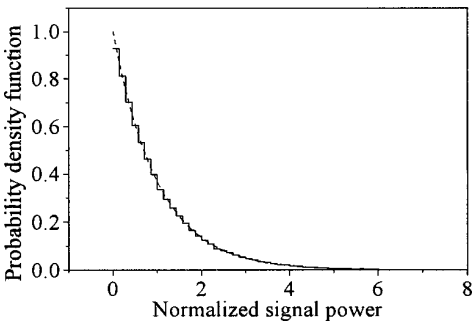

Fig. 4. Probability density distribution of the heterodyne signal power normalized to its mean value [$|I(t)|^2/P(t)$], compared with the expected negative exponential distribution (dashed curve).

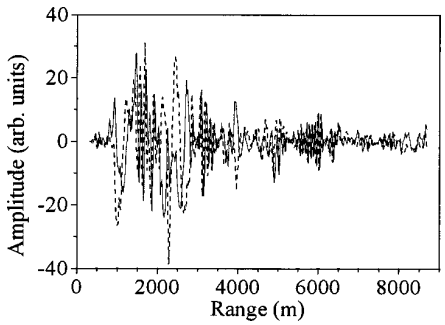

Fig. 5. One simulated signal realization corresponding to the models in Figs. 1 and 2, at $\lambda = 10.6\,\mu m$ and $\tau = 4\,\mu s$ ($l_p = 1200\,m$). The in-phase $J(t)$ (solid curve) and quadrature $Q(t)$ (dashed curve) components of the signal are presented. The sampling interval employed is $\Delta t_o(\Delta z_o) = 0.1\,\mu s$ (15 m).

The results from the simulations show that algorithms (14a) and (14b) allow one to retrieve the profile of $v(z)$ with a high spatial resolution but on the basis of a sufficiently large number of laser shots to reduce the error due to speckle noise. Thus the speckle noise limits the temporal resolution, i.e., the ability to observe rapid changes in atmospheric conditions. Because of the recurrence character of the algorithms, the noise-induced random error is accumulated and increases with the increase of $z - z_o$. The step of the increase is equal to the laser pulse length and consequently is longer at longer sensing pulses. However, in this case the noise-error increment per step is higher. Therefore one should use pulses with optimum length such that the increase of the noise error with $z - z_o$ is slow. Filtering the covariance estimate $\widehat{\mathrm{Cov}}(t, \theta)$ or the retrieved profile $v_r(z)$ of $v(z)$, or both, is an effective way to suppress the speckle-noise influence and thus to reduce the number of laser shots required to achieve a prescribed accuracy. Such an approach leads to improvement in the temporal resolution of retrieving $v(z)$ but is accompanied by some lowering of the spatial resolution. Hence the effective width of the filter window should have an optimum value, thus ensuring considerable noise suppression at an acceptable high spatial resolution.

In Figs. 6(a) and 6(b) we have represented the profiles of $v_r(z)$ restored by use of relations (14a) and (14b), respectively. These profiles correspond to the model of $v(z)$ described by Eq. (16). The laser wavelength and pulse length assumed are $\lambda = 10.6\,\mu m$ and $l_p = 1200\,m$, respectively. The number of simulated laser shots (signal realizations) is $N = 2000$. A $8\Delta t_o$- ($8\Delta z_o$)-wide-window moving average smoothing of $\widehat{\mathrm{Cov}}(t, \theta)$ and $v_r(z)$ is also performed. So the achievable resolution cell is $R \sim 8\Delta t_o (= 120\,m) \ll c\tau/2 (= 600\,m)$. It is shown in Figs. 6(a) and 6(b) that the speckle-noise effect accumulates with the increase in distance $z - z_o$. Also, it is noticeable that at longer distances ($z - z_o > 3$ km in the present case), algorithm (14a) is more affected by the speckle noise. At shorter distances from z_o ($z - z_o \sim$ several pulse lengths) both algorithms lead to acceptable accuracy of retrieving $v(z)$ even at narrower filter window and considerably smaller number of realizations (e.g., $N \sim 500$). The last property of the discussed algo-

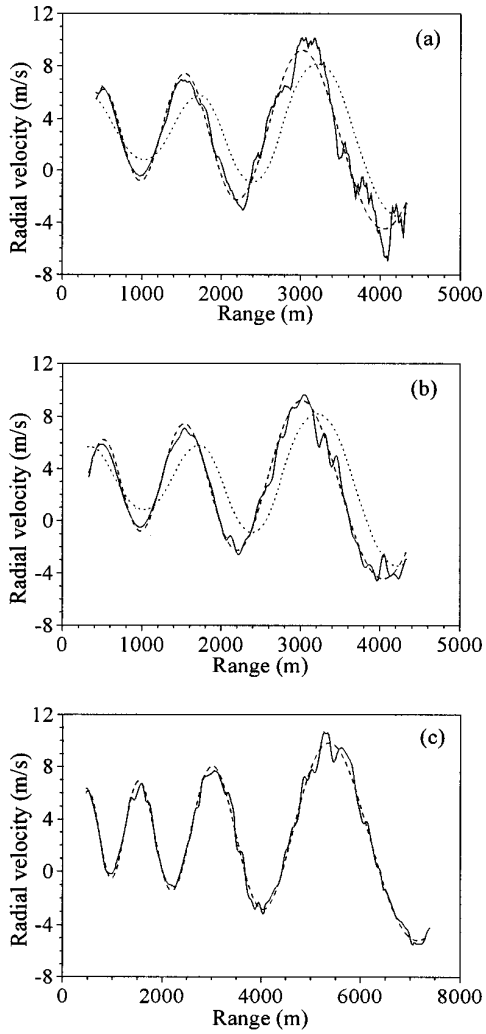

Fig. 6. Alternating radial wind velocity profiles $v_r(z)$ restored in the case of rectangular pulse (with $\lambda = 10.6\,\mu$m and $\tau = 4\,\mu$s) by use of (a) algorithm (14a), (b) algorithm (14b), and (c) algorithm (14a) and the lidar dead-zone scanning technique. The sampling interval employed is $\Delta t_o(\Delta z_o) = 0.1\,\mu$s (15 m). The number of signal realizations employed is (a) and (b) $N = 2000$ and (c) $N = 500$. $\widehat{\mathrm{Cov}}(t, \theta)$ and $v_r(z)$ are smoothed by a moving average with (a) and (b) $8\Delta t_o$- $(8\Delta z_o)$-wide window and (c) $4\Delta t_o$- $(4\Delta z_o)$-wide window. The original profile of $v(z)$ [described by Eq. (16)] is given for comparison by the dashed curve. The dotted curves in (a) and (b) represent the result obtained with the PP algorithm.

rithms suggests that a way to increase the range of remote sensing with high spatial and temporal resolution and accuracy is to progressively increase the lidar dead zone $[0, z_o]$. The simulations confirm the good results from such an approach of scanning (increasing step by step) the interval $[0, z_o]$ [see Fig. 6(c)]. The number of realizations employed in this case is $N = 500$, and $\widehat{\mathrm{Cov}}(t, \theta)$ and $v_r(z)$ are smoothed by a $4\Delta t_o$- $(4\Delta z_o)$-wide-window moving average ($R \sim 60$ m). As it is beyond the scope of this paper, we shall not discuss here any technical aspects regarding the scan of the lidar dead zone.

The dotted curves in Figs. 6(a) and 6(b) represent the profile of $v_r(z)$ corresponding to the same model of $v(z)$ [Eq. (16)] but obtained by using the PP algorithm.[11] The number of sampling points employed for averaging along the line of sight is $M = 20$. Thus the resolution cell achievable in this case is $R_{pp} \sim c(M\Delta t_o + \tau)/2 = c(20\Delta t_o + \tau)/2$; $\Delta t_o = 0.1\,\mu$s, $\tau = 4\,\mu$s. To reduce the speckle-noise effect, the covariance estimate $\widehat{\mathrm{Cov}}(t, \theta)$ is obtained by additional averaging over $N = 500$ realizations of $I(t)$. It can be seen that the resultant noise error is negligible, but there is a noticeable error due to the averaging along the line of sight and the finite pulse duration, i.e., as if the profile $v_r(z)$ is obtained by a R_{pp}-wide-window moving averaging of $v(z)$.

Profiles of $v_r(z)$ corresponding to the model of a wind vortex [Eq. (18)] and restored by the use of formulas (14a) and (14b) are shown in Figs. 7(a) and 7(b), respectively. They concern the case of $\lambda = 2\,\mu$m and $\tau = 0.2\,\mu$s, but the same are in practice the results for $\lambda = 10.6\,\mu$m and $\tau = 4\,\mu$s (see Ref. 25). In order to avoid excessive accumulation of the noise, the wind vortex area begins from the dead-zone end ($z = z_o$) and is covered by only several pulse lengths [$z - z_o \sim (2 - 3)c\tau/2$ when $\tau = 200$ ns and $\lambda = 2\,\mu$m, and $z - z_o \ll c\tau/2$ when $\tau = 4\,\mu$s and $\lambda = 10.6\,\mu$m]. Thus $v(z)$ is accurately retrieved on the basis of $N = 1000$ realizations $I_k(t)$ after filtering $\widehat{\mathrm{Cov}}(t, \theta)$ by a moving average with a $6\Delta t_o$-wide window ($R \sim 9$ m) when Eq. (14a) is used and a $4\Delta t_o$-wide window ($R \sim 6$ m) when Eq. (14b) is used. The same profile of

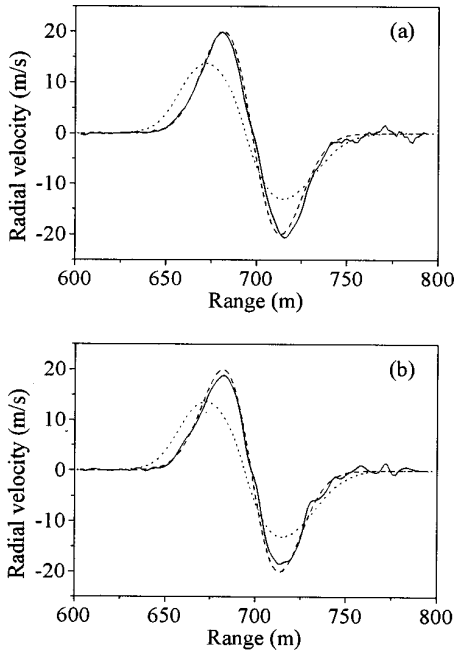

Fig. 7. Wind-vortex Doppler-velocity profiles $v_r(z)$ restored in the case of rectangular pulse (with $\tau = 0.2\,\mu$s and $\lambda = 2\,\mu$m) by use of (a) algorithm (14a) and (b) algorithm (14b). The sampling interval employed is $\Delta t_o(\Delta z_o) = 0.01\,\mu$s (1.5 m), and the number of signal realizations is $N = 1000$. $\widehat{\mathrm{Cov}}(t, \theta)$ and $v_r(z)$ are smoothed by a moving average with (a) $6\Delta t_o$- $(6\Delta z_o)$-wide window and (b) $4\Delta t_o$- $(4\Delta z_o)$-wide window. The original profile of $v(z)$ (dashed curve) and the profile obtained with the PP algorithm (dotted curve) are given for comparison.

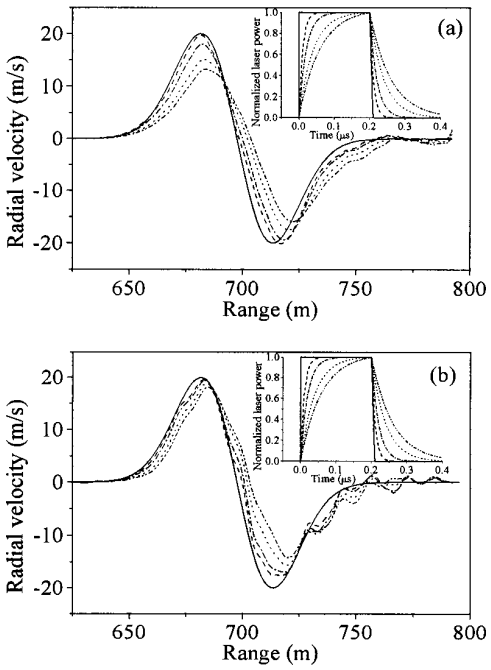

Fig. 8. Wind-vortex Doppler-velocity profiles $v_r(z)$ restored in the case of (inset) a rectangularlike pulse, with $\lambda = 2\,\mu$m, $\tau = 0.2\,\mu$s, and $\tau_r = 0.01\,\mu$s (dashed curve), 0.02 μs (dashed–dotted curve), 0.04 μs (dotted curve), 0.06 μs (dashed–double-dotted curve), by use of (a) algorithm (14a) and (b) algorithm (14b). The sampling interval employed is $\Delta t_o(\Delta z_o) = 0.01\,\mu$s (1.5 m). The number of signal realizations employed is $N = 1000$. $\widehat{\mathrm{Cov}}(t, \theta)$ and $v_r(z)$ are smoothed by a moving average with (a) $8\Delta t_o$- ($8\Delta z_o$)-wide window and (b) $4\Delta t_o$-($4\Delta z_o$)-wide window. The original profile of $v(z)$ is given for comparison by the solid curve.

$v(z)$ can be retrieved without noticeable statistical error by using a PP estimator at $M = 20$ and $N = 500$. However, as the minimal resolution cell in this case is $R_{pp} \sim 60$ m (of the order of the wind-vortex size), the final result for $v_r(z)$ is distorted with respect to $v(z)$ (see the dotted curves in Figs. 7(a) and 7(b) as well as Refs. 15 and 26 for more detail). The retrieved maximum-velocity magnitude is nearly two times smaller than the true one, and the positive-to-negative peak positions are separated by a distance different from the original one.

Since the rectangular pulse shape is usually some approximation of real pulse shapes, it is of interest to prove whether the approach developed here for rectangular pulses will lead to an acceptable recovery of $v(z)$ in the case of near-rectangular (rectangularlike) pulses. For this purpose we have considered the following rectangularlike pulse shape:

$$f(\vartheta) = \begin{cases} 0 & \text{for } \vartheta \leqslant 0 \\ D[1 - \exp(-\vartheta/\tau_r)] & \text{for } 0 \leqslant \vartheta \leqslant \tau, \\ \exp[-(\vartheta - \tau)/\tau_r] & \text{for } \tau < \vartheta \end{cases} \quad (20)$$

where $D = [1 - \exp(-\tau/\tau_r)]^{-1}$ and the quantities τ and τ_r may be interpreted as approximating rectangular pulse duration and rise (and decay) time, respectively. The signal realizations $I_k(t)$ corresponding to the above pulse shape are determined on the basis of Eq. (12a) at $\phi_h = \phi_{\mathrm{ch}} = \phi_o = 0$ and $\omega_o = \omega_h$. The covariance estimate $\widehat{\mathrm{Cov}}(t = t_{l_2} = 2z_{l_2}/c, \theta = m\Delta t_o)$ is obtained according to Eq. (19). Then, by using relations (14a) and (14b), we obtain two restored Doppler-velocity profiles $v_r(z)$. The results for $v_r(z)$ [compared with the true profile $v(z)$] corresponding to the model of the wind vortex described above [Eq. (18)] are represented in Figs. 8(a) and 8(b). It is assumed that the sensing radiation wavelength and the pulse duration are, respectively, $\lambda = 2\,\mu$m and $\tau = 0.2\,\mu$s. As may be expected, at relatively small rise (decay) time τ_r, an accurate restoration of $v(z)$ is achieved. The restoration error increases with the increase in τ_r but retains an acceptable value even at pulse shapes that have near-triangular form. The profiles of $v_r(z)$ obtained by use of the PP algorithm are in general more distorted [with respect to the true profile $v(z)$] than those obtained with the algorithms developed here. Only at relatively large values of τ_r, when the rectangularlike pulses become in fact triangularlike ones do the two types of distortions become comparable.

The simulations conducted show that the approach developed here of retrieving $v(z)$ permits one to reach a high spatial resolution without specifically decreasing the laser radiation wavelength, the pulse duration, and the sampling interval. At the same time, appropriate smoothing and lidar dead-zone scanning techniques as well as powerful lasers with high pulse-repetition rates should be used to ensure acceptable temporal resolution.

6. CONCLUSION

The inverse mathematic techniques developed in this study can be used successfully for retrieving high-range-resolution Doppler-velocity profiles on the basis of data obtained by coherent heterodyne Doppler lidars with (relatively long) rectangular and rectangularlike sensing laser pulses. These techniques allow one to achieve resolution scales that are considerably smaller than the pulse length. The techniques generalize some known techniques, including the PP algorithm, of determining Doppler-velocity profiles that are strictly valid only in the case of uniform aerosol velocity and concentration within line-of-sight intervals of the order of the pulse length.

The speckle noise is the main disturbing factor that leads to the appearance of noise in the final results. The use of a large number of laser shots provided by powerful lasers with high pulse-repetition rates is a way to suppress the noise and obtain accurate results. To avoid a too-large statistical volume, and thus to accelerate the measuring procedures (to improve the temporal resolution), one can essentially reduce the speckle-noise effect by filtering the autocovariance estimates and the recovered noisy profiles as well as by using the lidar dead-zone scanning technique.

ACKNOWLEDGMENT

This research was supported in part by the Bulgarian National Science Fund under grants F-907 and F-811.

Corresponding author L. Gurdev can be reached at the address on the title page or by e-mail, lugurdev@ie.bas.bg, or by fax, 359-2-975-3201.

REFERENCES

1. M. J. Post and R. E. Cupp, "Optimizing a pulsed Doppler lidar," Appl. Opt. **29**, 4145–4158 (1990).
2. R. Frehlich, S. M. Hannon, and S. W. Henderson, "Coherent Doppler lidar measurements of winds in the weak signal regime," Appl. Opt. **36**, 3491–3499 (1997).
3. A. V. Jelalian and R. M. Huffaker, "Laser Doppler techniques for remote wind velocity measurements," in *Specialist Conference on Molecular Radiation* (Marshall Space Flight Center, Huntsville, Ala., 1967), pp. 345–358.
4. R. Nordstrom, "A dual sensor role for pulsed CO_2 laser," Photonics Spectra **23**, 89–98 (1989).
5. S. M. Hannon and J. A. Thomson, "Aircraft wake vortex detection and measurement with pulsed solid-state coherent laser radar," J. Mod. Opt. **41**, 2175–2196 (1994).
6. S. W. Henderson, C. P. Hale, J. R. Magee, M. J. Kavaya, and A. V. Huffaker, "Eye-safe coherent laser radar system at 2.1 μm using Tm, Ho:YAG lasers," Opt. Lett. **16**, 773–775 (1991).
7. R. Targ, B. C. Steakley, J. G. Hawley, L. L. Ames, P. Forney, D. Swanson, R. Stone, R. G. Otto, V. Zarifis, Ph. Brockman, R. S. Calloway, S. H. Klein, and P. A. Robinson, "Coherent lidar airborne wind sensor. II. Flight-test results at 2 and 10 μm," Appl. Opt. **35**, 7117–7127 (1996).
8. L. L. Gurdev, T. N. Dreischuh, and D. V. Stoyanov, "Deconvolution techniques for improving the resolution of long-pulse lidars," J. Opt. Soc. Am. A **10**, 2296–2306 (1993).
9. T. N. Dreischuh, L. L. Gurdev, and D. V. Stoyanov, "Lidar profile deconvolution algorithms for some rectangular-like laser pulse shapes," in *Advances in Atmospheric Remote Sensing with Lidar*, A. Ansmann, R. Neuber, P. Raioux, and U. Wandinger, eds. (Springer-Verlag, Berlin, 1996), pp. 135–138.
10. E. V. Stoykova, L. L. Gurdev, B. M. Bratanov, M. D. Angelova, and D. V. Stoyanov, "Low Doppler velocity estimation in infrared coherent lidars," in *Proceedings of the 15th International Laser Radar Conference*, Part II (Institute of Atmospheric Optics, Tomsk, Russia, 1990), pp. 413–417.
11. K. S. Miller and M. M. Rochwarger, "A covariance approach to spectral moment estimation," IEEE Trans. Inf. Theory **IT-18**, 588–596 (1972).
12. M. R. Harris and D. V. Willets, "Performance characteristics of a TE CO_2 laser with a long excitation pulse," in *Coherent Laser Radar: Technology and Applications*, Vol. 12 of 1991 OSA Technical Digest Series (Optical Society of America, Washington, D.C., 1991), pp. 5–7.
13. L. L. Gurdev, T. N. Dreischuh, and D. V. Stoyanov, "High-resolution processing of long-pulse-lidar data," NASA Conf. Publ. **3158**, 637–640 (1992).
14. A. Dabas, Ph. Salamitou, D. Oh, M. Georges, J. L. Zarader, and P. H. Flamant, "Lidar signal simulation and processing," in *Proceedings of the Seventh Conference on Coherent Laser Radar: Applications and Technology*, P. H. Flamant, ed. (Ecole Polytechnique, Paris, 1993), pp. 221–228.
15. Ph. Salamitou, A. Dabas, and P. Flamant, "Simulations in the time domain for heterodyne coherent laser radar," Appl. Opt. **34**, 499–506 (1995).
16. J. Y. Wang, "Heterodyne laser radar SNR from a diffuse target containing multiple glints," Appl. Opt. **21**, 464–476 (1982).
17. A. Ishimaru, *Wave Propagation and Scattering in Random Media, Vol. 1: Single Scattering and Transport Theory* (Academic, New York, 1978).
18. A. E. Siegman, "The antenna properties of optical heterodyne receivers," Appl. Opt. **5**, 1588–1594 (1966).
19. J. H. Churnside and H. T. Yura, "Speckle statistics of atmospherically backscattered laser light," Appl. Opt. **22**, 2559–2565 (1983).
20. G. M. Ancellet and R. T. Menzies, "Atmospheric correlation-time measurements and effects on coherent Doppler lidar," J. Opt. Soc. Am. A **4**, 367–373 (1987).
21. J. W. Goodman, *Statistical Optics* (Wiley, New York, 1985).
22. R. M. Measures, *Laser Remote Sensing: Fundamentals and Applications* (Wiley, New York, 1984).
23. V. I. Tatarski, *Wave Propagation in Turbulent Atmosphere* (Nauka, Moscow, 1967).
24. I. N. Bronstein, K. A. Semendjajew, *Taschenbuch der Mathematik* (Gemeinschaftsausgabe Verlag Nauka, Moskau; BSB B. G. Teubner Verlagsgesellschaft, Leipzig, Germany, 1989).
25. B. T. Lottman and R. G. Frehlich, "Evaluation of coherent Doppler lidar velocity estimators in nonstationary regimes," Appl. Opt. **36**, 7906–7918 (1997).
26. T. N. Dreischuh, L. L. Gurdev, and D. V. Stoyanov, "Intercomparison between two approaches for improving the resolution of Doppler-velocity coherent-lidar profiles," in *Tenth International School on Quantum Electronics: Laser Physics and Applications*, P. A. Atanasow and D. V. Stroyanov, eds., Proc. SPIE **3571**, 272–276 (1999).